Materials Advances

ROYAL SOCIETY OF CHEMISTRY

PAPER

View Article Online
View Journal | View Issue

Cite this: *Mater. Adv.*, 2022, 3, 5096

Surface-enhanced luminescence of Cr^{3+}-doped $ZnAl_2O_4$ and $MgAl_2O_4$ using $Ag@SiO_2$ and $Au@SiO_2$ core–shell nanoparticles†

Rodrigo A. Valenzuela-Fernández, *[a] Julien Cardin, *[b] Xavier Portier,[b] Christophe Labbé,[b] Camilo Segura,[c] Víctor Vargas,[a] Antonio Galdámez[a] and Igor O. Osorio-Román[d]

Received 25th February 2022,
Accepted 20th May 2022

DOI: 10.1039/d2ma00217e

rsc.li/materials-advances

In this study, we investigate chromium-doped spinels (CDSs) and their characteristic red photoluminescence (PL) due to the strong crystal field and octahedral coordination geometries of the Cr^{3+} ions. An increase in the luminescence efficiency of the CDSs caused by the interaction with plasmon excitation is studied to achieve more efficient luminescence. We successfully synthesise CDSs using the citrate sol–gel method and metallic nanoparticles (MNPs) using the classical citrate reduction method. In addition, we cover the MNPs with silica shells, which are used to modify the surface. The surface-enhanced effect exerted by the surfaces modified with $Ag@SiO_2$ and $Au@SiO_2$ core–shell nanoparticles on the PL of the two CDSs is studied. The silica shell of the MNPs is used as a separator between the $MNPs@SiO_2$-modified surface and the CDS. An enhancement of the PL is found for the CDS coupled to MNPs compared with the uncoupled CDSs. The PL enhancement factors and lifetimes are also investigated. The interaction between the CDSs and MNPs is investigated, and several factors are found to influence the PL of the CDSs. The main mechanism explaining the PL enhancement is proposed. A better understanding of the surface-enhanced luminescence of the CDSs may lead to further improvements in these systems.

1. Introduction

Spinels such as $ZnAl_2O_4$ (ZAO) and $MgAl_2O_4$ (MAO) have advantageous electrical, mechanical, magnetic, optical, and catalytic properties.[1–3] These oxides, doped with small amounts of Cr^{3+}, can be found in nature as red cubic crystals[4] and used as paint additives to lower the temperature of objects exposed to sunlight.[5] Under controlled growth conditions, changing the synthesis method and parameters, such as temperature or dopant concentration, can lead to different sizes, morphologies, and luminescent properties of inorganic phosphors.[6–8] Inorganic phosphors, such as spinels, consist of a crystalline host material doped with a small amount of rare earth elements or transition metal ions, such as Eu^{3+} [9] or Cr^{3+}.[3,6,8] Cr^{3+} is widely used as a dopant for the development of tunable lasers, displays, and bioimaging.[10] Cr^{3+} has a $3d^3$ electronic configuration and exhibits photoluminescence (PL) emission from either the ^2E or the $^4T_2$ excited state. The emission depends on the strength of the crystal field environment surrounding the Cr^{3+} ion,[11] which can be divided into two categories: the low-field host matrix resulting in a spin-allowed transition of $^4T_2 \rightarrow {}^4A_2$ (green emission) or the high-field host matrix resulting in the R-lines spin-forbidden transition of $^2E \rightarrow {}^4A_2$ (red/pink emission).

Many fundamental and applied studies have been conducted on the interaction of plasmon resonances generated in metallic nanostructures with luminescent centers[12–16] or optical interactions. The latter can be studied by using techniques, such as surface-enhanced Raman scattering (SERS), surface-enhanced fluorescence (SEF), and metal-enhanced phosphorescence (MEP).[17–22] SEF has been widely studied for organic molecules and some inorganic luminophores, such as quantum dots,[23–25] whereas MEP has been studied using organic dyes[19,20] and organometallic complexes at room temperature.[21,22]

[a] *Departamento de Química, Facultad de Ciencias, Universidad de Chile, P.O. Box 653, Chile. E-mail: rvalenzuelafer@uchile.cl*
[b] *CIMAP, CEA, CNRS, UMR6252, Normandie Université, ENSICAEN UNICAEN, 14050, Caen Cedex 4, France. E-mail: julien.cardin@ensicaen.fr*
[c] *Center for Soft Matter Research, SMAT-C, Universidad de Santiago de Chile, Avenida Bernardo O'Higgins 3363, Santiago, Chile*
[d] *Instituto de Ciencias Químicas, Facultad de Ciencias, Universidad Austral de Chile, Isla Teja, P.O. Box 567, Valdivia, Chile*

† Electronic supplementary information (ESI) available: SEM and BSE images, extinction spectra of colloidal solutions, frequency domain intensities decays and data fits of emission and excitation spectra. See DOI: https://doi.org/10.1039/d2ma00217e

In the previously mentioned studies luminescent compounds with excited-state lifetimes were used within the nanosecond time range. However, compounds with longer excited-state lifetimes exist, such as inorganic phosphors with variable lifetime ranges depending on their atomic composition.[26] For instance, the excited-state lifetimes in some Cr^{3+}-doped inorganic phosphors have been reported to be in the millisecond time range.[27–29] To the best of our knowledge, surface-enhanced luminescence (SEL) of inorganic phosphors has not been studied. In this work, we report on the SEL of two chromium-doped spinels (CDSs) with lifetimes in the millisecond range at room temperature. We present the synthesis of two CDSs: $ZnAl_2O_4$:Cr^{3+} (ZAOC) and $MgAl_2O_4$:Cr^{3+} (MAOC), deposited on the surface of two types of core–shell metallic nanoparticles (MNPs), namely, Ag@SiO_2 and Au@SiO_2. Furthermore, the SEL of rare-earth-doped NPs coupled with MNPs and an inverse-opal-structured substrate show promising upconversion results.[30,31] Finally, we study the effect of the core–shell MNP surfaces on the spectroscopic properties of absorption and PL by comparing with the corresponding properties of a similar surface without the core–shell MNPs.

2. Experimental

2.1. Materials

A Coors® alumina crucible (50 mL), Corning® glass 2947, $Zn(NO_3)_2{\cdot}6H_2O$ (≥99.5% pure), $Cr(NO_3)_3{\cdot}9H_2O$ (99%), anhydrous citric acid (≥99.5%), tetraethylorthosilicate (TEOS, 98%), $KAuCl_4$ (98%), (3-aminopropyl)trimethoxysilane (APTMS, 97%), sodium silicate solution, poly(2-(dimethylamino)ethyl methacrylate) solution 20 wt% (PDMAEMA) and ammonium hydroxide solution (28.0–30.0 wt%) were purchased from Sigma-Aldrich (USA). $Al(NO_3)_3{\cdot}9H_2O$ (98.5%), $Mg(NO_3)_2{\cdot}6H_2O$ (>99%), $AgNO_3$ (99.8%), absolute ethanol, 2-propanol, NaOH, HCl (37 wt%) and HNO_3 (65 wt%) were acquired at Merck (Germany).

2.2. Spinel synthesis

Spinels were synthesised by using the citrate sol–gel method described by Abdukayum *et al.*[32] The molar ratio of citric acid to total metal ions was 1.5 : 1. ZAO and MAO, corresponded to spinels of zinc (Zn) and magnesium (Mg), respectively, with aluminum (Al) and a molar ratio of A : Al (A = Zn or Mg) of 1 : 2. ZAOC and MAOC corresponded Zn : Al : Cr and Mg : Al : Cr spinels, respectively, and both spinels had a molar ratio of 2 : 4 : 1.

Scheme 1 shows the synthetic steps for all the materials. The synthetic process for obtaining the spinels involved mixing citric acid and the metal ions in Milli-Q water at pH 5, and the pH was adjusted by adding an ammonia hydroxide solution. The mixture was then stirred vigorously for 2 h at room temperature. The mixture was heated at 70 °C to form a gel. Once the gel was formed, the product was dried at 130 °C for 3 h and heated again at 200 °C for 7 h. After this process, a powder was obtained, milled in an Agata mortar, and annealed in air in an alumina crucible at 1000 °C for 3 h. The final material was a white powder for both ZAO and MAO and a slightly pink powder for both ZAOC and MAOC.

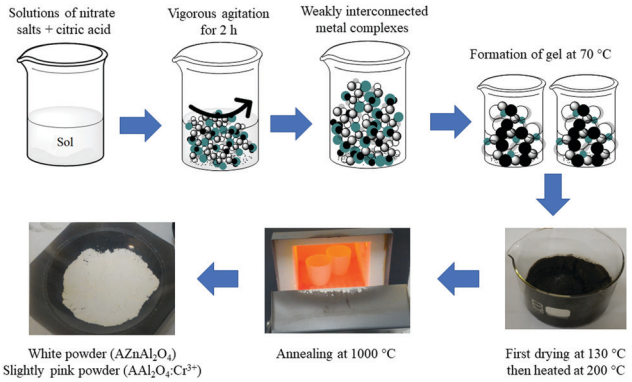

Scheme 1 Representation of the citrate sol-gel synthesis. (A = Zn or Mg).

2.3. Synthesis of Ag@SiO_2 and Au@SiO_2 core–shell NPs

Ag@SiO_2 and Au@SiO_2 core–shell MNPs were synthesized using the method described by Segura *et al.*[33] with a few modifications. The synthesis of AgNPs (silver NPs) was based on the protocols described by Lee–Meisel.[34] $AgNO_3$ (18 mg) was dissolved in 100 mL of Milli-Q water, the solution was boiled; and 2 mL of trisodium citrate (38.8 mM) was added. This solution was boiled for 1 h until the colour of the solution changed from colourless to silver-grey, and then, it was cooled to room temperature. The final product was a colloidal suspension of AgNPs, which were centrifuged for 10 min at 1000 rpm. The supernatant was then collected for further analysis.

For the AgNP coating, 45 mL of the colloidal supernatant was mixed with 200 mL of ethanol in an amber bottle. Then, 1.5 mL of 30% (w/v) ammonia and 300 μL of TEOS (40 mM) were added. The solution was agitated for 5 min and then allowed to settle for 60 h. After 60 h, the solution was centrifuged for 45 min at 5000 rpm, and the precipitated material (Ag@SiO_2) was collected and dispersed in Milli-Q water.

AuNPs (gold NPs) were obtained by dissolving 20 mg of $KAuCl_4$ in 100 mL of Milli-Q water. The solution was brought to a boil; and 5 mL of trisodium citrate (38.8 mM) was added. This solution was boiled for 1 h until the colour of the solution changed from colourless to wine red, and then, it was cooled to room temperature. The final product was a colloidal suspension of AuNPs, which were centrifuged for 10 min at 1000 rpm. The supernatant was then collected for further analysis.

For the AuNP coating, 50 mL of the colloidal solution of AuNPs was transferred to a 250 mL Erlenmeyer flask and 4 mL of APTMS (1 mM) was added. The solution was stirred for 30 min at room temperature. Then, the temperature was raised to 90 °C, and 6 mL of sodium silicate 0.54% (w/v) was added under constant stirring and left for 4 h. The colloidal solution was then cooled down to room temperature and centrifuged for 45 min at 5000 rpm. The precipitate material (Au@SiO_2) was collected and dispersed in Milli-Q water.

2.4. Surface modifications

Ag@SiO_2 and Au@SiO_2 were deposited on a Corning® Glass 2947. First, the glass slides were cleaned using aqua regia for

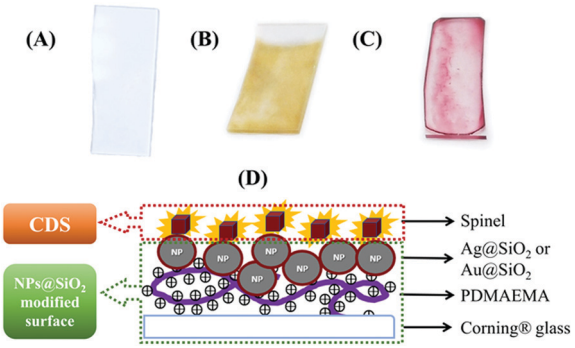

Scheme 2 Surface modification schemes. (A) Cleaned Corning® glass; (B) Ag@SiO_2; (C) Au@SiO_2; (D) Scheme describing the ensemble formed with deposited spinels and MNPs-modified surfaces.

3 h, rinsed with deionised water, and submerged in a 1 M NaOH solution for 30 min. Then, the glass slides (Scheme 2(A)) were rinsed with deionised water and dried. The dry glass was submerged in a 0.5 vol% Solution of PDMAEMA for 15 min and then rinsed with deionised water. The active glass slides were dried and stored at room temperature. This process activates the glass surface with positive charges, which allows deposition of the Ag@SiO_2 NPs that are negatively charged by electrostatic attraction on the glass slides. The glass slides with PDMAEMA were submerged in an Ag–colloidal solution for 12 h. The glass slides were washed, dried, and stored in a closed container in a moisture-free atmosphere. Scheme 2(B) shows a glass slide of an Ag@SiO_2 NPs core–shell modified surface (AgMS).

For the Au@SiO_2 deposition, we used dried PDMAEMA-functionalised glass slides and dropped 30 μL of the Au@SiO_2 colloidal solution. The surfaces were then dried in a closed container at room temperature and stored for later use. Scheme 2(C) shows a glass slide of an Au@SiO_2 NPs core–shell modified surface (AuMS).

2.5. Samples preparation for photoluminescence studies

For the samples used in the PL experiments, and the photoluminescence excitation (PLE) and time-resolved PL (TRPL) measurements, we prepared a 0.2% (w/v) dispersion of the spinels in 2-propanol. These suspensions were sonicated for 30 min and then allowed to rest for 10 min to allow the larger particles to settle. For the samples devoted to the PL and PLE measurements, we took an aliquot of the supernatant with a Pasteur pipette and dropped it onto the PDMAEMA-functionalised glass slides. For lifetime measurements, a 30 μL aliquot of the supernatant was added to the PDMAEMA-functionalised and MNP-functionalised glass slides by spin coating them at 1000 rpm for 30 s. Scheme 2(D) shows a schematic representation of the spinels deposited on the MNP-MS; henceforth, we refer to them as ensembles.

2.6. Characterisation

Scanning electron microscopy-energy-dispersive X-ray spectroscopy (SEM-EDX) was performed using a Bruker Tescan Vega 3 scanning electron microscope equipped with a Quantax 400 EDS spectrometer. Cylindrical pellets were prepared by uniaxially pressing polycrystalline powder samples at approximately 5 × 108 Pa. They were coated with an Au–Pd sputtering system. The samples were mounted on double-sided carbon tape and adhered to an Al specimen holder for analysis.

Powder X-ray diffraction (PXRD) patterns were collected at room temperature in the 2θ range of 5°–80° using a Bruker D8 ADVANCE powder diffractometer (Bruker, Billerica, MA, USA) with CuKα radiation (λ = 1.54178 Å). The PXRD patterns were indexed using the CHEKCELL computer program.

Conventional transmission electron microscopy (TEM) and high-resolution transmission electron microscopy (HRTEM) were performed on the spinels using a double-corrected cold FEG ARM 200F microscope operated at 200 kV. TEM analyses of the Ag@SiO_2 and Au@SiO_2 core–shell MNPs were performed using a Hitachi HT7700 system operating at 120 kV (Hitachi, Tokyo, Japan). In both cases, the powder was mixed with *n*-butanol, and a drop of the resulting suspension was deposited on a copper grid (300 mesh) with a carbon film containing holes, and the grid was dried before loading it on the TEM specimen holder. The digitalised images were processed using DigitalMicrograph® software (GATAN).

Atomic force microscopy (AFM) was performed using a WiTec Alpha 3000 with a 75 kHz tip in tapping mode. AFM micrographs were taken, discarding edges and less homogeneous areas.

Continuous-wave (CW) PL measurements were performed at room temperature by using an Innova 90C argon laser (excitation wavelength 514 nm) at 100 mW, an incident angle of 45°, and a beam spot size of approximately 1 mm^2 and chopped at 3 Hz. The emitted photons were collected into a light cone of 28° through a set of lenses and dispersed using a Horiba Jobin–Yvon Triax 180 monochromator. The detection was ensured by an R5108 Hamamatsu photomultiplier tube connected to an SR830 lock-in amplifier referenced at the excitation light-chopper frequency. SEL measurements were performed at room temperature with an ISS-PC1 photon counting spectrofluorimeter using an optical arrangement in which the emission was observed in the same plane as the excitation (front face). The excitation source was a violet laser diode emitting at 405 nm with an output power of 20 mW. A 570 nm longpass filter was used.

For the extinction spectra of the colloidal solutions, core–shell solutions, and core–shell MNPs deposited on glass, ultraviolet-visible studies were carried out using a double-beam Shimadzu UV-1800 spectrophotometer in specular transmission mode.

Lifetime measurements were performed at room temperature using a Chronos FD with an emission detector Model R928 PMT by Hamamatsu. The excitation light source was a 405 nm LED with a 530 nm long-pass filter. The emission detector wavelength ranged from 240 to 900 nm.

3. Results and discussion

3.1. SEM-EDS, X-ray diffraction and HRTEM analyses

SEM was used to analyse the powder samples. The SEM and backscattered electron (BSE) images are shown in the ESI,†

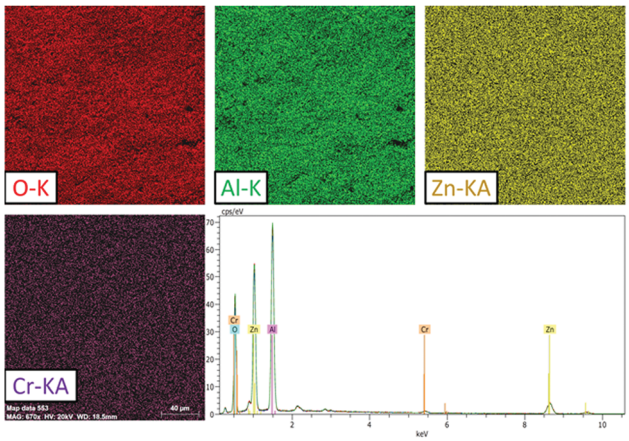

Fig. 1 ZAOC SEM results: O, Al, Zn, and Cr EDS chemical mapping (20 kV) and typical EDS spectrum of the area shown by the chemical maps.

(Fig. S1). Fig. S1 (ESI†) shows a homogeneous growth from a morphological point of view in the compounds and shows no apparent difference between one grain and another. Fig. 1 shows a typical SEM-EDX image of the ZAOC sample and reveals that the samples are homogeneous throughout the scanned area (217 × 212 μm). In addition, the elemental mapping images reveal that all the constituent atoms are uniformly distributed throughout the material.

The PXRD patterns are presented in Fig. 2. The PXRD patterns are fully consistent with those of the $Fd\bar{3}m$ space group, and the cell parameters are summarised in Table 1. All compounds crystallised in the well-known spinel-type structure according to the standard Joint Committee on Powder Diffraction (JCPDS) cards No. 01-070-8182 (ZAO and ZAOC) and No. 04-008-3488 (MAO and MAOC). Fig. 2 shows the reaction products were of the nominal composition of AAl_2O_4:Cr^{3+} (A = Zn, Mg). Additionally, there were only single phases within the detection limits, and secondary phases or impurity peaks were not detected. A comparison of the Cr-doped and undoped samples confirms that Cr^{3+} doping does not change the crystalline structure and that there is no apparent distortion caused by Cr^{3+}.

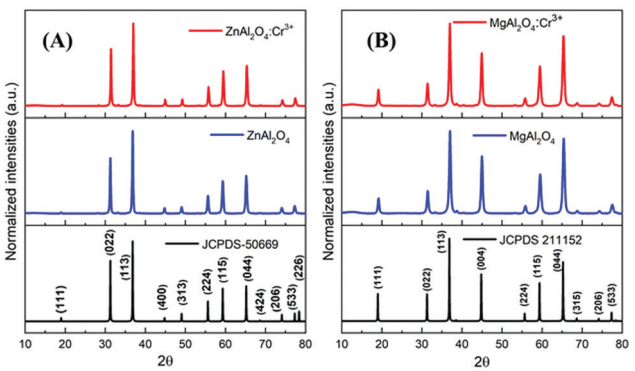

Fig. 2 PXRD patterns of Cr-doped and undoped $ZnAl_2O_4$ (A) and $MgAl_2O_4$ (B). The bottom diagrams are the reference XRD data of the corresponding spinels.

The crystallite sizes (t) were calculated using Scherrer's equation[35]

$$t = \frac{K\lambda}{\beta \cos \theta} \quad (1)$$

where t is the crystallite size (nm), K is the correction factor, which was taken to be equal to 1, λ is the X-ray wavelength (CuKα, nm), β is the full width at half maximum (FWHM, radians) of the (113) X-ray diffraction plane and θ is the corresponding Bragg diffraction angle. Table 1 lists the mean t values. Additionally, we observe that the lattice parameter and the volumes of the unit cells are very similar in the spinels with and without Cr, which supports that there is no change in the spinel crystal structure due to the addition of Cr. Furthermore, we found that the two families of spinels (ZAO-ZAOC and MAO-MAOC) have comparable sizes, but the Mg-based spinels, which are approximately 20 nm, are smaller than the Zn-based spinels, which are approximately 31 nm.

TEM and HRTEM images and the corresponding fast Fourier transform (FFT) patterns are displayed in Fig. 3 for all the samples. We observed that the ZAO and ZAOC spinels have larger grains (average 64.5 nm and 52.5 nm, respectively) in comparison to the MAO and MAOC spinels (average 17.2 nm and 16.0 nm, respectively). The ZAO and ZAOC crystallite sizes found from the TEM images differed from those estimated using the Scherrer equation (Table 1). The difference may stem from PXRD data that characterise a large volume of material being used for the Scherrer equation, and the TEM technique only considers the volume of a few grains (the grain size values were obtained by averaging 40 grains). A more probable explanation for the difference is the presence of stacking faults in the ZAO and ZAOC grains, leading to smaller sizes from PXRD than those observed using TEM. The grain sizes for MAO and MAOC (17.2 nm and 16.0 nm, respectively) obtained by using TEM were consistent with the crystallite sizes determined by using the Scherrer equation. The single-grain micrographs (Fig. 3(ii) and (iii)) show a crystalline ordering symmetry that is consistent with the spinel crystal structure. All the FFTs of the single-grain micrographs are in agreement with cubic symmetry (fcc to be more precise).[36] Fig. 4 shows the TEM images of single-crystal MNPs and core–shell MNP colloidal solutions. The AgNPs (Fig. 4(A)) had diameters of approximately 50 nm and the Ag@SiO_2 (Fig. 4(B)) had diameters of about 100 nm, indicating that the silica shell thickness was approximately 25 nm. Alternatively, the diameters of the AuNPs (Fig. 4(C)) were less than 20 nm and the Au@SiO_2 (Fig. 4(D)) had diameters of

Table 1 Experimental lattice parameters and crystallite size

Sample	a [Å]	Volume [Å]	t^a [nm]	t^b [nm]
ZAO	8.0926(43)	529.99(75)	31.118(20)	64.5
ZAOC	8.0948(13)	530.42(22)	31.935(21)	52.5
MAO	8.0867(50)	528.83(87)	19.449(31)	17.2
MAOC	8.0931(52)	530.08(90)	20.896(30)	16.0

[a] Size calculated by using the Scherrer equation. [b] Size obtained from HRTEM.

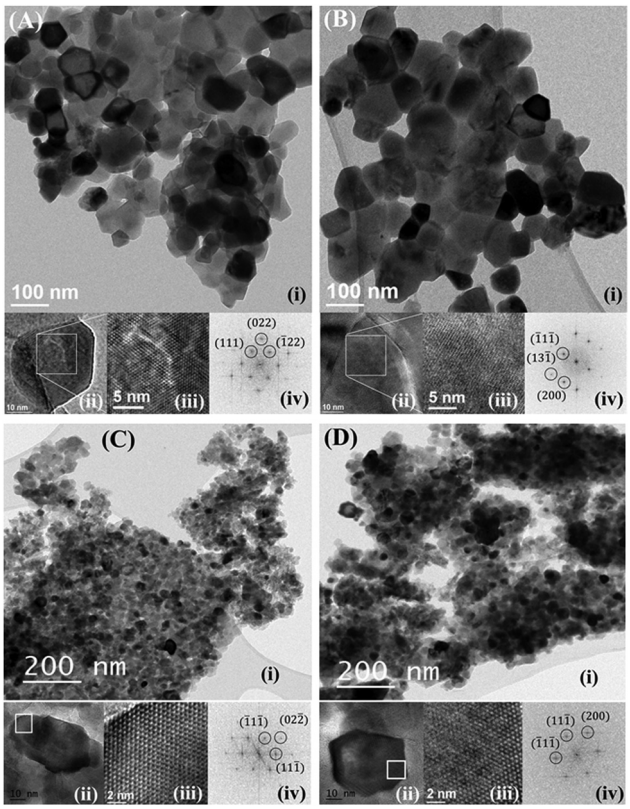

Fig. 3 TEM and HRTEM images and the corresponding FFT for (A) ZAO; (B) ZAOC; (C) MAO; (D) MAOC. In each figure, (i) shows crystals; (ii) image of a crystal; (iii) shows a magnification of (ii), and (iv) is a FFT of (iii) (showing the following crystallographic projections [0$\bar{1}$1], [1$\bar{1}\bar{2}$], [110], [110], for ZAO, ZAOC, MAO and MAOC, respectively).

approximately 40 nm, indicating that the silica shell thickness was approximately 10 nm.

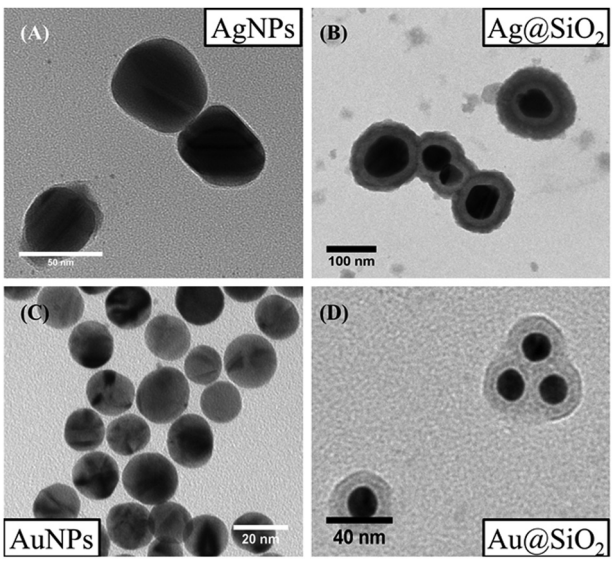

Fig. 4 Bright field TEM images of MNPs. (A) AgNPs; (B) Ag@SiO_2; (C) AuNPs; (D) Au@SiO_2.

3.2. Photoluminescence

Fig. 5 shows the PL and PLE measurements of the CDSs ZAOC and MAOC. The PL and PLE spectra were also fit using the Lorentzian function (Fig. 5, red-dashed lines), and the data describing the measured bands are reported in Table S1 (ESI†). The ZAOC PL spectrum (Fig. 5(A), left-hand side) contains several narrow bands that are characteristic of emission from a Cr^{3+} with octahedral coordination geometry in a strong crystal field.[37–39] Although the band with the highest intensity appears at 14124.3 cm^{-1} (708 nm), the most important band appears at 14534.8 cm^{-1} (688 nm) and corresponds to the R-line, called the zero-phonon line (ZPL). The ZPL is marked with a green arrow in Fig. 5, and is related to the $^2E \rightarrow {}^4A_2$ transition.[6,37–50] The lower energy band next to the ZPL, at 14287.1 cm^{-1} (700 nm) corresponds to the N_2-line.[38,39,47–50] In addition, several studies[37–39,48,49] indicated that the bands appearing at 13915.6 and 14124.3 cm^{-1} (719 and 708 nm) correspond to Stokes phonon sidebands (PSB), whereas others studies[40,42,46,47,51] reported them as different N-lines. The bands appearing at

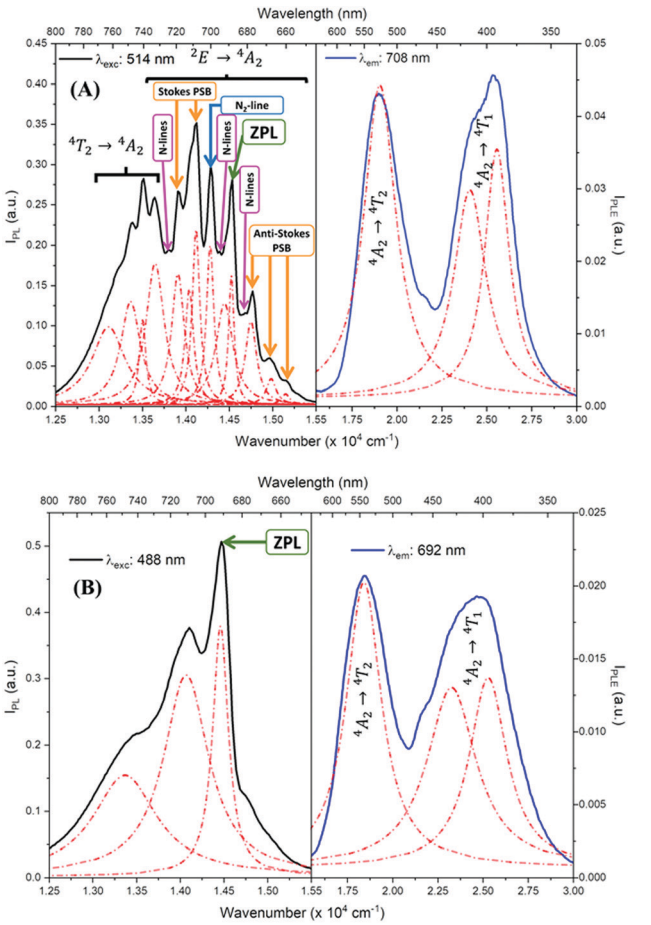

Fig. 5 PL (black) and PLE (blue) spectra of (A) ZAOC and (B) MAOC. The red-dashed lines represent Lorentzian fits. The green arrow indicates the zero-phonon line, the blue arrow indicates the N_2-line, and the orange arrows indicate Stokes and anti-Stokes phonon sidebands (PSB). The pink arrows indicate different N-lines that appear when the concentration of Cr^{3+} is ~0.2 mol%.

14757.3, 14990.9 and 15157.0 cm^{-1} (678, 667, and 660 nm, respectively) are anti-Stokes PSB.[37–39,48,49] Both Stokes and anti-Stokes PSB are related to vibrionic transitions.[37–39,48,49] The bands at lower energies of 13113.4, 13369.2, 13506.9, and 13651.8 cm^{-1} (763, 748, 740, and 733 nm, respectively) were also reported as N-lines,[51] but there is evidence[38,42,48] that these bands correspond to the $^4T_2 \rightarrow {}^4A_2$ transition. Finally, the ZAOC PL spectrum also depicts small bands located at 13812.1, 14388.5, and 14684.3 cm^{-1} (724, 695, and 681 nm, respectively), marked with pink arrows. These bands correspond to N-lines as well and appear when the Cr^{3+} concentration is $\sim$0.2 mol%.[4,41]

R- and N-lines originate at the atomic scale in the crystal of the compounds. In normal-type spinels, depending on the oxidation state, the cations can adopt octahedral or tetrahedral coordination geometry.[52] In the ideal case, the Al atoms adopt octahedral geometries (16d positions), whereas the Zn or Mg atoms adopt tetrahedral geometries (8a positions). Because Cr atoms have a +3 oxidation state, they are more likely to adopt octahedral geometries.[46,47,52] Nevertheless, occasional defects may occur in the crystal lattice, and the atoms conforming to normal-type spinels can exchange positions to adopt an inverse spinel, where some Al atoms occupy 8a positions and some Zn atoms occupy 16d positions.[46,47] The R-lines observed in the ZAOC emission spectrum are associated with the 16d positions of the normal spinel, whereas the N-lines are associated with Cr^{3+} ions that are in inversion sites between Zn^{2+} and Al^{3+} within the first two coordination spheres.[46,47] This explanation also applies in the $^4T_2 \rightarrow {}^4A_2$ transition appearing at lower energies because the Cr^{3+} ions located in the inversion sites lie in weakly, tetrahedrally coordinated crystal field sites.[38]

In contrast, the intensities of R- and N-lines depend on the Cr^{3+} concentration in spinels.[4] According to Loan *et al.*,[6] when the Cr^{3+} concentration is approximately 0.1 mol%, the R-line (14534.8 cm^{-1}) should be the most intense in the PL spectrum. However, when the Cr^{3+} concentration is approximately 8 mol%, the band with the highest intensity appears at 14124.3 cm^{-1}, which is similar to the band found in the ZAOC PL spectrum. This result supports that the Cr^{3+} concentration in the CDS is 5 mol%. Furthermore, when the concentration exceeds 16 mol%, the lattice parameters increase slightly (not observed here), which implies a decrease in the crystal field environment around the octahedrally-coordinated Cr^{3+} ion, and the R- and N-lines sidebands disappear.

In MAOC PL spectrum (Fig. 5(B), left-hand side), the most intense band at 14471.8 cm^{-1} (691 nm) can be attributed to ZPL and is due to the $^2E \rightarrow {}^4A_2$ transition. The bands at 13495.3 and 14104.4 cm^{-1} (741 and 709 nm) can be ascribed to an R-line side band.[53,54] The R-line is due to a Cr^{3+} transition when the cation has an octahedral coordination geometry in a strong crystal field, whereas the N-line is due to the perturbation of Cr^{3+} owing to the inversion of Mg^{2+} and Al^{3+} in the first two coordination spheres.[4,10,53–55]

The PLE spectra (Fig. 5, right-hand side) reveal two broad bands between 15500.0 and 30000.0 cm^{-1}. For both spinels, the bands at approximately 18500.0 cm^{-1} are related to the $^4A_2 \rightarrow {}^4T_2$ transition, and the bands at approximately 25000.0 cm^{-1} correspond to the $^4A_2 \rightarrow {}^4T_1$ transition.[10,42,45,46,53,55,56] At higher annealing temperatures, the $^4A_2 \rightarrow {}^4T_1$ transition band appears with a higher intensity than that of the $^4A_2 \rightarrow {}^4T_2$ transition band.[55]

Table S1 (ESI†) lists data from the fits. The ZAOC PL spectrum (Fig. 5(A), left-hand side) presents two doublets for the two bands that have shoulders. One doublet is at 14046.7 and 14124.2 cm^{-1}, which is related to the R-side band as mentioned earlier, and the other one is the R-line, located at 14451.9 and 14532.1 cm^{-1}. The doublet found in the R-line is well described in the literature as R1 and R2 bands, which are usually well resolved at low temperatures.[4,37,41,43,45] The bands observed in the MAOC PL spectrum (Fig. 5(B), left-hand side) fit well three bands. In addition, in both PLE spectra (Fig. 5, right-hand side), the fit for the $^4A_2 \rightarrow {}^4T_1$ transition band contained two bands around 23232.7 and 25355.1 cm^{-1}, which is due to the $^4T_1$ state splitting into the $^4T_1(t_2^2e^1)$ and $^4T_1(t_2^1e^2)$ states. This phenomenon manifests as shoulders peaks in the PLE spectra.[48,50,55,57]

Using the observed excitation bands, we evaluated the crystal field splitting parameter, D_q, and Racah parameters B and C, according with the following equations:[53,56]

$$10D_q = \nu_1 \quad (2)$$

$$B = \frac{(2\nu_1 - \nu_2)(\nu_2 - \nu_1)}{27\nu_1 - 15\nu_2} \quad (3)$$

$$9B + 3C = \nu_3 \quad (4)$$

The ν_1, ν_2, and ν_3 frequencies represent $^4A_2 \rightarrow {}^4T_2$, $^4A_2 \rightarrow {}^4T_1$ and $^2E \rightarrow {}^4A_2{}^2E \rightarrow {}^4A_2$ transitions, respectively, in cm^{-1}. For both doped spinels, the value used for ν_3 was the energy of the zero-phonon line. The values obtained are listed in Table 2 and compared with values previously reported in the literature.[46,53] The D_q/B values for both CDSs are similar and greater than 3, indicating that the Cr^{3+} ions are in strong crystal field sites because $D_q/B < 2.3$ for weak field sites and $D_q/B > 2.3$ for strong field sites. Additionally, the D_q/B values are in the expected range for Cr^{3+} in octahedral coordination geometry.[46,53]

3.3. Luminescence enhancement

3.3.1. Characterization of the MSs. The extinction spectra of the MNP colloidal solutions are shown in Fig. S2 (ESI†). For the AgNP colloidal solution, the maximum resonance extinction peak was located at 24390.2 cm^{-1} (410 nm) and presents a redshift to 23310.0 cm^{-1} (429 nm) for Ag@SiO_2. A similar result was found for the AuNP colloidal solution where the maximum resonance extinction peak was at 19267.8 cm^{-1} (519 nm) and there was a redshift to 18975.3 cm^{-1} (527 nm) for Au@SiO_2.

Table 2 Experimental crystal field parameters

Sample	D_q [cm^{-1}]	B [cm^{-1}]	C [cm^{-1}]	D_q/B
ZAO	1898(6)	604(6)	3032(31)	3.14(5)
ZAOC	1842(6)	622(6)	2957(31)	2.96(5)
MAO	1869	534	3236[a]	3.50[a]
MAOC	1815	545	3225	3.33

[a] Values calculated here, not informed by Singh *et al.*[46]

In both cases, this shift was due to the silica coating, as shown in Fig. 4. In addition, we changed the coating of MNPs from citrate to silica. Consequently, the refractive index changes because silica decreases the refractive index of the MNPs and produces a redshift[58,59] in the maximum resonance extinction peak. Nevertheless, when the silica coated MNPs, Ag@SiO_2 and Au@SiO_2, were deposited on glass, AgMS and AuMS, respectively, the refractive index changed because MNPs were surrounded by air instead of water. This effect produced a blueshift[33,60] of both silica-coated MNPs, from 23310.0 cm^{-1} (429 nm) to 23980.8 cm^{-1} (417 nm) for Ag@SiO_2 and from 18975.3 cm^{-1} (527 nm) to 19157.1 cm^{-1} (522 nm) for Au@SiO_2. In addition to serving as a protective cap, the SiO_2 coating served as separator between MNPs and CDS because SEL is sensitive to the luminophore–MNP distance. Some optimal luminophore–MNP distances for SEL studies were found to be greater than 2 nm and even up to 10 nm.[61–63] In addition, an increase in the PL was also found when a fluorophore was near the MNP surface using cationic and anionic polyelectrolytes as a separator instead of SiO_2. This is known as layer-by-layer technique. The average height of each layer (monolayer) is approximately 3 nm,[64–66] and enhancement factors had been found up to 10-fold the PL when 10 layers (or 5 bilayers) are used on these MSs.[67] Therefore, the luminophore was separated from the metal surface by least at 30 nm. Moreover, if a luminophore is located too close to the MNP surface, non-radiative decay processes prevail and luminescence quenching occurs.[16,68,69] Furthermore, the SEL effect is the most pronounced when the plasmon resonance of the MNPs is spectrally coincident with (i) the extinction/absorption of the luminescent species near the surface, and (ii) the wavelength excitation source. The latter is because the plasmonic surface absorption cross-section scatters the incident electromagnetic radiation to the luminophore and enhances its luminescence.[23,69] This effect allows the absorption band to excite electrons to upper levels, where radiative recombination may occur. At the excitation wavelength, the MNP-MS exhibits a local field enhancement that increases the electromagnetic energy volumetric density. If a luminophore exists near that area, this enhancement creates additional localised energy, which increases locally the excitation of the luminophore. The total extinction energy is usually shared between absorption, heat conversion, and scattering energy, and is redistributed in space. Fig. 6 shows the normalised extinction spectra of both the SiO_2-coated MNPs on glass and the normalized PLE of CDS. We observed a significant overlap for both Cr^{3+} ion transitions, $^4A_2 \rightarrow {}^4T_1$ and $^4A_2 \rightarrow {}^4T_2$, in the extinction spectra for both NP@SiO_2 core–shell MSs. A violet laser diode at 405 nm should be enough to produce SEL of CDSs.

Fig. 7 shows typical AFM images of MNPs@SiO_2 MSs. The AgMS are more separated from each other (Fig. 7(A)) and are more homogeneously distributed compared to the AuMS (Fig. 7(B)), which are aggregated. This is a consequence of the preparation methods. The glass was dipped into the Ag@SiO_2 colloidal solution, whereas the colloidal solution of Au@SiO_2 was dropped onto the glass instead. Additionally, the height profiles of the AFM images are shown in Fig. 7. The AgMS has a height profile similar in size to the observed AgNP TEM image. In contrast, the AuMS has a higher height profile than the observed size of the AuNP by TEM image (Fig. 4(D)) because the Au@SiO_2 particles aggregate on this surface.

3.3.2. Surface-enhanced luminescence. Based on the assumption that the same quantity of emitting centers were present in both silica-coated NPs-MSs and CDSs, the SEL can be determined using the enhancement factor (EF) described by eqn (5):

$$\mathrm{EF} = \frac{\int I_{\mathrm{MS\text{-}CDS}}}{\int I_{\mathrm{CDS}}} \quad (5)$$

where $\int I_{\mathrm{MS\text{-}CDS}}$ is the integral of the emission intensity for the ensemble formed by silica-coated MNP-MS and CDS and $\int I_{\mathrm{CDS}}$ is the integral of the emission intensity of CDS. Fig. 8 shows SEL spectra of the CDSs at room temperature. This figure displays the ZPL previously identified in Fig. 5. Additionally, MNP-MSs do not produce a blue- or redshift in the PL spectra. For the ZAOC PL spectrum, there are two transitions; therefore, we calculated the EF for each transition. Moreover, the EF values found were approximately 2.4, which indicated that the MNP-MSs can enhance the luminescence and PL efficiency of the CDSs at room temperature and may enhance another luminescent inorganic phosphor.

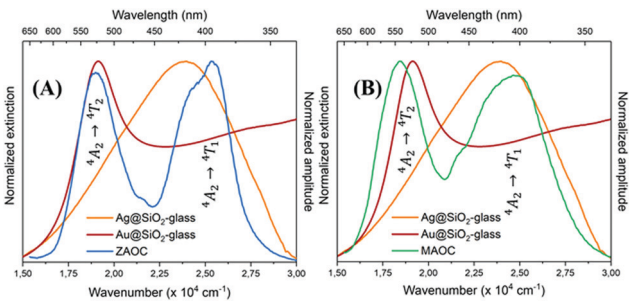

Fig. 6 Normalised extinction spectra of AgMS (orange) and AuMS (red) with normalised PLE spectra of (A) ZAOC (blue) and (B) MAOC (green).

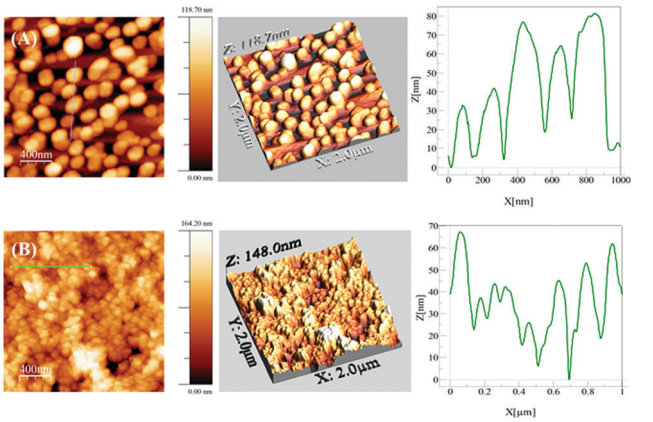

Fig. 7 AFM images and height profiles of the silica coated MNPs on glass for (A) AgMS; (B) AuMS. For both MS, we can see the 2D AFM images (left); 3D AFM images (center); and height profiles (right). The lines on the 2D AFM images are related to the respective height profiles.

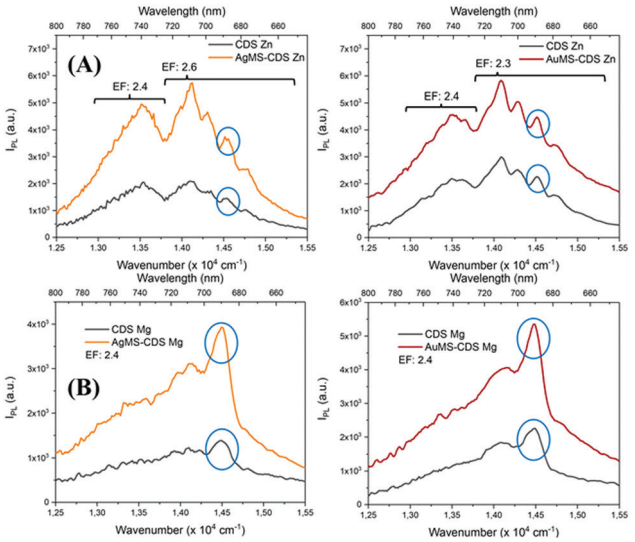

Fig. 8 SEL spectra of (A) ZAOC and (B) MAOC on $Ag@SiO_2$ (orange) and $Au@SiO_2$ (red) MSs and their counterparts without MSs (black). The blue circle indicates the ZPL.

3.4. Lifetimes

The frequency-domain (FD) model was used to measure the lifetimes, as previously described.[70–72] For this technique, the excitation light intensity is modulated with varying angular frequency ω, and both excitation and modulated emission are recorded. The phase shift P and the relative modulation M of the emission are calculated from these data, and the lifetime is determined using models of time decay as single, multi, or average exponential. The resulting measured phase and the modulation values were analysed by using the multi-exponential time-dependent model given by eqn (6)

$$I(t) = \sum_i \alpha_i e^{\frac{-t}{\tau_i}} \quad (6)$$

where τ_i is the lifetime and α_i is the preexponential factor. The contribution of each component to the intensity of the stationary state due to exponential decay is given by eqn (7)

$$f_i = \frac{\alpha_i \tau_i}{\sum_j \alpha_j \tau_j} \quad (7)$$

where f_i is the fractional contribution to the total luminescence emission and $\sum f_i = 1$.[73] The average lifetime is given by eqn (8)

$$\langle \tau \rangle = \sum f_i \tau_i \quad (8)$$

The FD measurement fits are shown in the ESI† (Fig. S3 and S4). The best fits were obtained with two-exponential decay models, leading to the smallest values of χ^2 for ZAOC and MAOC with both $MNPs@SiO_2$ ensembles at room temperature. Table 3 reports the lifetime results. For all the ensembles, the average lifetimes were in the millisecond range, with the shortest lifetimes for the MAOC ensembles. For the ZAOC sets, we compared the different lifetime values for the CDS with $Ag@SiO_2$ or $Au@SiO_2$ core–shell MNPs and without MNPs. We observed comparable lifetime values, with a higher value for the $Ag@SiO_2$ ensemble than that of the $Au@SiO_2$ ensemble. For the MAOC samples, we observed an increase in the lifetimes for both $MNPs@SiO_2$ ensembles. In addition, either in the absence or presence of $MNPs@SiO_2$, τ_1 is larger than τ_2 for both CDSs. The same trend was repeated for the fractional contributions, where f_1 was larger than f_2, except for the ZAOC-$Au@SiO_2$ ensemble. Previous literature[48,50,74,75] has shown that the emission of Cr^{3+} ions for different spinels is in the millisecond range, and the lifetime values obtained for these compounds were directly proportional to the annealing duration and temperature.[38,50,75]

Table 3 Two-component lifetimes and fractional intensities of CDSs on different MSs

CDS	τ_1 [ms]	τ_2 [ms]	τ [ms]	f_1	f_2	α_1	α_2	χ^2
ZAOC								
NP-free	1.29(2)	0.0201(5)	1.09	0.840(2)	0.160	65	792	2.14
AgMS	2.31(2)	0.0186(10)	1.55	0.670(1)	0.330	29	1778	2.52
AuMS	1.38(2)	0.0126(8)	0.532	0.380(1)	0.620	27.5	4937	1.18
MAOC								
NP-free	0.90(1)	0.0182(10)	0.725	0.802(1)	0.198	89.2	1089	1.86
AgMS	0.910(6)	0.0510(20)	0.852	0.933(1)	0.067	103	130	1.69
AuMS	1.33(2)	0.00828(4)	0.816	0.611(1)	0.389	45.9	4693	1.97

3.5. Interaction between the CDSs and MNPs

When the MNPs are near luminescent emitters, the PL intensity is modified in two ways. First, the incident light excites the surface plasmon resonance (SPR) of the MNPs. Emitters localised in regions of near-field enhancement are subject to enhanced excitation light and manifest an increased excitation rate. Moreover, the radiative decay rate of the emitter is influenced by the modification of the localised density of states (LDOS) introduced by the MNPs through the well-known Purcell effect.[76–78] Second, the emitters in an excited state can recombine through a nonradiative decay channel, emitting photons directly to the far-field (PL), or relax rapidly by exciting the localised plasmon resonance of the MNPs *via* the energy transfer channel (Förster energy transfer). The relaxation *via* the plasmon resonance increases with the shortening of the MNP-emitter distance and leads to radiative phenomena or nonradiative recombination. The radiative rate occurring with SPR is associated with the far-field radiation emitted (scattered) by the accelerating and decelerating charged particles. The ratio of this radiative rate to the total recombination rate usually increases with the NP size.[79,80] The nonradiative rate (absorption) has been previously studied,[81–83] where several mechanisms were shown to contribute to this rate: electron–electron (e–e) scattering, electron–phonon (e–p) scattering, electron-defects (e–d), and damping due to surface effect (e–s).

For the ensembles, the CDS emitters were deposited on the surface of the $MNPs@SiO_2$ core–shell which were located on a glass slide surface with SiO_2 acting as a spacer between the MNPs and CDSs. This ensemble can be considered an emitter–MNP hybrid system, and the excitation and emission processes can be described as a donor (emitter)–acceptor (MNP) system. Scheme 3 shows this CDS-MNP system in two configurations

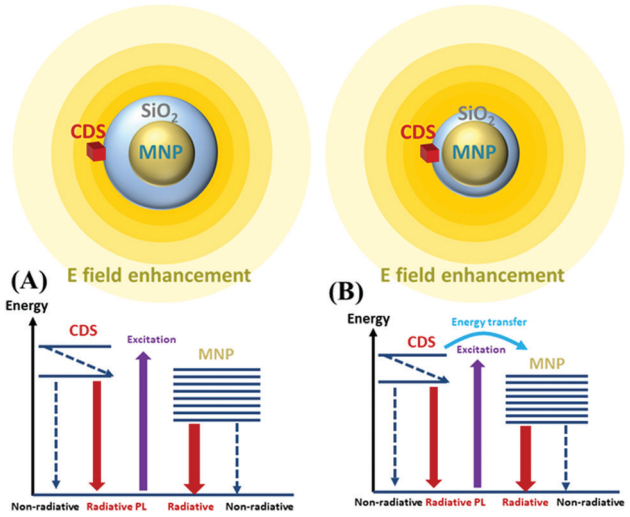

Scheme 3 Representation of the donor-acceptor system with the excitation and emission processes of the CDS-MNP surface hybrid system. (A) a large shell thickness and (B) a short shell thickness are shown.

with a larger shell thickness (Scheme 3(A)) of a few tens of nanometers and a smaller shell thickness (Scheme 3(B)) of a few nm.

We observed an enhancement in the luminescence of the CDSs in the presence of MNPs with an EF of $\sim$2.4. Moreover, we observed time decays with one slow component in the millisecond range and one fast component in the tens of nanosecond range, which are comparable for CDSs in the absence of MNPs and the ensembles. We examined the luminescence enhancement using the theoretical arguments developed for this subject. First, in the low photon flux approximation, the emission intensity, mainly due to the $^2E \rightarrow {}^4A_2$ transition, is proportional to the excitation rate Γ_{exc} (in s^{-1}) and to the quantum yield (QY) according to eqn (9)

$$I_{PL} \propto \Gamma_{exc} QY \tag{9}$$

An increase in PL emission in the presence of MNPs is then either related to an increase in Γ_{exc}, QY, or both. The excitation rate can be expressed as the product of the emitter emission ($^2E \rightarrow {}^4A_2$ transition) cross-section σ_{emi} (in cm^2) and photon flux $\phi_{h\nu}$ (in cm^{-2} s^{-1}). The emission cross-section can be considered an intrinsic property that remains unchanged. On the other hand, in a medium with MNPs, the photon flux can locally fluctuate because of the localized electromagnetic field enhancement, leading to a locally enhanced photon flux, $\phi^*_{h\nu}$. In the case of the Ag@SiO_2 and Au@SiO_2 core–shell MNPs, it was reported[84] that, depending on their surroundings, the refractive index, and shell thickness up to 40 nm, the electromagnetic field enhancement extends up to the external interface of the shell and beyond. In the ensemble, the QY can be strongly modified by the CDS–MNP distance, which is a key parameter because it influences the CDS–MNP interaction.

Two distinct situations are usually described according to the distance between emitters (CDSs) and MNPs, as shown in Scheme 3. The first situation occurs when CDSs are located far from the MNPs or when the MNPs are not on MSs. The intrinsic and nonperturbed quantum yield of CDSs (QY^0) can be given by eqn (10)

$$QY^0 = \frac{\Gamma_r^0}{\Gamma_r^0 + \Gamma_{nr}^0} \tag{10}$$

with intrinsic radiative (Γ_r^0) and nonradiative (Γ_{nr}^0) rates. Both Γ_r^0 and Γ_{nr}^0 are considered unaffected because they are determined by the transition probability and oscillator strength. In the second situation, that is, when the CDSs are close to the MNPs (an ensemble), the interdistances are smaller than a few nm,[85] therefore the quantum yield of the CDSs when it is near the MNPs (QY*) is given by eqn (11)

$$QY^* = \frac{\Gamma_r^0 + \Gamma_r^m}{\Gamma_r^0 + \Gamma_r^m + \Gamma_{nr}^0 + \Gamma_{ET}} \tag{11}$$

where Γ_r^0 is the intrinsic unperturbed radiative rate for the CDSs far from the MNPs, Γ_r^m is the modified radiative rate for the CDSs close to the MNPs, Γ_{nr}^0 is the nonradiative rate assumed to not be perturbed, and Γ_{ET} is the energy transfer rate (Förster). Γ_{ET} can be divided into the radiative rate of the localised plasmon resonance in the ensemble (Γ_r^{MNP}) and the nonradiative rates of the localised plasmon resonance of the ensemble (Γ_{nr}^{MNP}). This latter is the major channel leading to the different damping processes (e–e, e–p, e–d, e–s), therefore, Γ_{ET} is considered a quenching term for the CDSs.

The CDS lifetimes (τ) in an MS without MNPs are described only as a function of Γ_r^0 and Γ_{nr}^0 given by eqn (12)

$$\tau = \frac{1}{\Gamma_r^0 + \Gamma_{nr}^0} \tag{12}$$

When the CDSs form an ensemble, eqn (12) can be rewritten as eqn (13)

$$\tau = \frac{1}{\Gamma_r^0 + \Gamma_r^m + \Gamma_{nr}^0 + \Gamma_{ET}} \tag{13}$$

As mentioned before, assuming a low photon flux approximation, the emission intensity (PL) is proportional to Γ_{exc} times QY (eqn (9)). The increase in PL emission in the presence of MNPs can be attributed to either an increase in Γ_{exc}, an increase in QY, or both. However, the time decays found here has two components for both CDSs without MNPs and in an ensemble with an MS, while a modification of QY should result in different time constants, according to eqn (10) and (13). For this reason, based on our experimental results, we can assume that the increase in the PL is mainly due to an increased excitation rate, with no obvious change in quantum efficiency. Thus, the CDSs had unmodified quantum efficiencies and decay times but benefitted from the increase in the excitation rate induced by the presence of metal particles. In the CDS–MNP systems, the minimum distance between the CDSs and MNPs was obtained owing to the outer shell of SiO_2 being 25 nm for Ag@SiO_2 and 10 nm for Au@SiO_2. This distance is approximately ten times larger than the optimal fluorophore MNP distance reported for SEL.[85] For these reasons, we did not

observe QY modification that would occur at short distances (~1–2 nm), but rather an increased excitation rate that might be due to electromagnetic field enhancement, which takes place at a distance equivalent to the SiO_2 shell thickness.

4. Conclusions

In this work, we investigated the SEL when CDS interacts with MNPs at room temperature. The citrate sol–gel synthesis yielded homogeneous and crystalline inorganic materials or spinels. The Cr^{3+} dopant in spinel matrices did not significantly change the crystal lattice parameters. The backscattered images and EDS elemental analyses showed a uniform distribution of Zn, Mg, Al, and Cr (concentration ~5% mol) atoms in the samples.

The Lorentzian fitting of the ZAOC PL spectrum showed a characteristic doublet of the R-line, whereas the Lorentzian fitting of the PLE spectra showed splitting of the $^4A_2 \rightarrow {}^4T_1$ transition band. The most intense band found in the ZAOC PL spectrum was an R-line sideband at 14124.3 cm^{-1}, instead of the R-line (zero phonon line) band at 14534.8 cm^{-1}. Finally, the evaluation of the crystal field parameters indicated that the Cr^{3+} ions in the CDSs were in a strong crystal field environment.

We obtained PLE spectra for the CDSs deposited on a metallic silica-coated NP surface, at room temperature. We monitored the bands with the highest intensities and found that the enhancement factor values were approximately 2.4 for both MAOC and ZAOC spinels. However, the average lifetime values $\langle\tau\rangle$ were not significantly altered when the CDSs were near Ag@SiO_2 and Au@SiO_2. Thus, the results showed that obtaining enhanced luminescence for compounds with lifetimes higher than the nanosecond range at room temperature is possible. We believe that this enhancement is governed by an enhancement of the local electromagnetic field in the vicinity of the core–shell MNPs rather than an energy transfer induced by QY modification. This study paves the way for new studies on PL enhancement based on the SEL effect using rare-earth-doped phosphor.

Author contributions

The manuscript was prepared and written with the contributions of all authors. All authors approved the final version of the manuscript.

Conflicts of interest

There are no conflicts to declare.

Acknowledgements

Rodrigo thanks ANID (ex-CONICYT) National PhD Scholarship 21150816. Camilo thanks ANID (ex-CONICYT) National PhD Scholarship 21150397. Antonio thanks to ANID-FONDECYT 1190856. Igor thanks to ANID-FONDECYT 1190246. The authors thank the Chilean-French International Associated Laboratory for 'Multifunctional Molecules and Materials' (LIAM3-CNRS N°1027).

Notes and references

1 F. Zerarga, A. Bouhemadou, R. Khenata and S. Bin-Omran, *Solid State Sci.*, 2011, **13**, 1638–1648.
2 G. Fan, J. Wang and F. Li, *Catal. Commun.*, 2011, **15**, 113–117.
3 C. Wang, A. H. Shen and Y. Liu, *J. Lumin.*, 2020, **227**, 117552.
4 D. L. Wood, G. F. Imbusch, R. M. Macfarlane, P. Kisliuk and D. M. Larkin, *J. Chem. Phys.*, 1968, **48**, 5255–5263.
5 P. Berdahl, S. S. Chen, H. Destaillats, T. W. Kirchstetter, R. M. Levinson and M. A. Zalich, *Sol. Energy Mater. Sol. Cells*, 2016, **157**, 312–317.
6 T. T. Loan and N. N. Long, *VNU J. Sci. Math. - Phys.*, 2018, **34**, 1–7.
7 M. M. Golsheikh, A. M. Arabi and M. S. Afarani, *Mater. Res. Express*, 2019, **6**, 125052.
8 D. Zhang, J. Chen, C. Du, B. Zhu, Q. Wang, Q. Shi, S. Cui and W. Wang, *Front. Mater. Sci.*, 2020, **14**, 73–80.
9 Y.-C. Lin, M. Karlsson and M. Bettinelli, *Top. Curr. Chem.*, 2016, **374**, 21.
10 C. Pratapkumar, S. C. Prashantha, H. Nagabhushana and D. M. Jnaneshwara, *J. Sci. Adv. Mater. Devices*, 2018, **3**, 464–470.
11 M. G. Brik, J. Papan, D. J. Jovanović and M. D. Dramićanin, *J. Lumin.*, 2016, **177**, 145–151.
12 K. Sokolov, G. Chumanov and T. M. Cotton, *Anal. Chem.*, 1998, **70**, 3898–3905.
13 J. Gersten and A. Nitzan, *J. Chem. Phys.*, 1981, **75**, 1139–1152.
14 T. Ming, L. Zhao, Z. Yang, H. Chen, L. Sun, J. Wang and C. Yan, *Nano Lett.*, 2009, **9**, 3896–3903.
15 S. A. Camacho, P. H.-B. Aoki, P. Albella, O. N. Oliveira, C. J.-L. Constantino and R. F. Aroca, *J. Phys. Chem. C*, 2016, **120**, 20530–20535.
16 F. Tam, G. P. Goodrich, B. R. Johnson and N. J. Halas, *Nano Lett.*, 2007, **7**, 496–501.
17 C. D. Geddes and J. R. Lakowicz, *J. Fluoresc.*, 2002, **12**, 121–129.
18 R. Aroca, G. J. Kovacs, C. A. Jennings, R. O. Loutfy and P. S. Vincett, *Langmuir*, 1988, **4**, 518–521.
19 Y. Zhang, K. Aslan, S. N. Malyn and C. D. Geddes, *Chem. Phys. Lett.*, 2006, **427**, 432–437.
20 Y. Zhang, K. Aslan, M. J.-R. Previte, S. N. Malyn and C. D. Geddes, *J. Phys. Chem. B*, 2006, **110**, 25108–25114.
21 M. J.-R. Previte, K. Aslan, Y. Zhang and C. D. Geddes, *J. Phys. Chem. C*, 2007, **111**, 6051–6059.
22 M. Meng, F.-L. Zhang, J. Yi, L.-H. Lin, C.-L. Zhang, N. Bodappa, C.-Y. Li, S.-J. Zhang, R. F. Aroca, Z.-Q. Tian and J.-F. Li, *Anal. Chem.*, 2018, **90**, 10837–10842.
23 M. Ramírez-Maureira, V. Vargas, A. Riveros, P. J.-G. Goulet and I. O. Osorio-Román, *Mater. Chem. Phys.*, 2015, **151**, 351–356.

24 E. Konstantinova, A. Zyubin, V. Slezhkin, V. Bryukhanov, K. Matveeva, E. Moiseeva and I. Samusev, *Biophotonics—Riga 2017*, 2017, 24.
25 K. Jia, L. Yuan, X. Zhou, L. Pan, P. Wang, W. Chen and X. Liu, *RSC Adv.*, 2015, **5**, 58163–58170.
26 P. Vitta, P. Pobedinskas and A. Zukauskas, *IEEE Photonics Technol. Lett.*, 2007, **19**, 399–401.
27 D. Chen, X. Chen, X. Li, H. Guo, S. Liu and X. Li, *Opt. Lett.*, 2017, **42**, 4950.
28 K. Tsuchiya, K. Sako, N. Ishiwada and T. Yokomori, *Meas. Sci. Technol.*, 2020, **31**, 065005.
29 A. Wadhwa, C. Wang, C. Wang, R. Ma, X. Qiao, X. Fan and G. Qian, *J. Am. Ceram. Soc.*, 2018, **102**, jace.16098.
30 B. Shao, Z. Yang, Y. Wang, J. Li, J. Yang, J. Qiu and Z. Song, *ACS Appl. Mater. Interfaces*, 2015, **7**, 25211–25218.
31 Y. Wang, Z. Yang, Y. Ma, Z. Chai, J. Qiu and Z. Song, *J. Mater. Chem. C*, 2017, **5**, 8535–8544.
32 A. Abdukayum, J.-T. Chen, Q. Zhao and X.-P. Yan, *J. Am. Chem. Soc.*, 2013, **135**, 14125–14133.
33 C. Segura, V. Vargas, R. A. Valenzuela-Fernández, C. S. Danna and I. O. Osorio-Román, *ACS Appl. Energy Mater.*, 2020, **3**, 7680–7688.
34 P. C. Lee and D. Meisel, *J. Phys. Chem.*, 1982, **86**, 3391–3395.
35 B. D. Cullity and S. R. Stock, *Elements of X-Ray Diffraction*, Pearson Education Limited, 3rd edn, 2014.
36 D. B. Williams and C. B. Carter, *Transmission Electron Microscopy*, Springer US, Boston, MA, 2009.
37 A. Bessière, S. Jacquart, K. Priolkar, A. Lecointre, B. Viana and D. Gourier, *Opt. Express*, 2011, **19**, 10131–10137.
38 D. N. Hebbar, S. G. Menon, K. S. Choudhari, S. A. Shivashankar, C. Santhosh and S. D. Kulkarni, *J. Am. Ceram. Soc.*, 2018, **101**, 800–811.
39 D. Zhang, Q. Guo, Y. Ren, C. Wang, Q. Shi, Q. Wang, X. Xiao, W. Wang and Q. Fan, *J. Sol-Gel Sci. Technol.*, 2018, **85**, 121–131.
40 K. Tanaka, K. Hirao, T. Ishihara and N. Soga, *J. Ceram. Soc. Jpn.*, 1993, **101**, 102–104.
41 H. M. Kahan and R. M. Macfarlane, *J. Chem. Phys.*, 1971, **54**, 5197–5205.
42 G. Rani, *Powder Technol.*, 2017, **312**, 354–359.
43 W. Mikenda and A. Preisinger, *J. Lumin.*, 1981, **26**, 67–83.
44 H. H. Luc, T. K. Nguyen, V. M. Nguyen, A. Suchocki, A. Kamińska, V. K. Le, V. H. Nguyen and T. T. Luong, *Acta Phys. Pol., A*, 2003, **104**, 581–587.
45 W. Nie, F. M. Michel-Calendini, C. Linarès, G. Boulon and C. Daul, *J. Lumin.*, 1990, **46**, 177–190.
46 V. Singh, R. P.-S. Chakradhar, J. L. Rao and H.-Y. Kwak, *J. Mater. Sci.*, 2011, **46**, 2331–2337.
47 D. Zhang, Y. H. Qiu, Y. R. Xie, X. C. Zhou, Q. R. Wang, Q. Shi, S. H. Li and W. J. Wang, *Mater. Des.*, 2017, **115**, 37–45.
48 H. G. S. Karthik, S. G. Menon, D. Hebbar, K. S. Choudhari, C. Santhosh and S. D. Kulkarni, *Mater. Res. Bull.*, 2019, **111**, 294–300.
49 S. G. Menon, D. N. Hebbar, S. D. Kulkarni, K. S. Choudhari and C. Santhosh, *Mater. Res. Bull.*, 2017, **86**, 63–71.
50 S. G. Menon, K. S. Choudhari, S. A. Shivashankar, C. Santhosh and S. D. Kulkarni, *J. Alloys Compd.*, 2017, **728**, 484–489.
51 T. T. Loan, L. H. Ha and N. N. Long, *VNU J. Sci. Math. - Phys.*, 2010, **26**, 37–42.
52 A. R. West, *Solid State Chemistry and its Applications, Students Edition*, John Wiley & Sons, Ltd, Chichester, West Sussex, United Kingdom, 2nd edn, 2014.
53 Y. Hao, S. Wang and K. Zhang, *Mater. Chem. Phys.*, 2020, **253**, 123323.
54 T. L. Phan, S. C. Yu, M. H. Phan and T. P.-J. Han, *J. Korean Phys. Soc.*, 2004, **45**, 63–66.
55 N. T.-K. Chi, N. V. Quang, N. T. Tuan, N. D.-T. Kien, D. Q. Trung, P. T. Huy, P. D. Tam and D. H. Nguyen, *J. Electron. Mater.*, 2019, **48**, 5891–5899.
56 A. R. Molla, C. R. Kesavulu, R. P.-S. Chakradhar, A. Tarafder, S. K. Mohanty, J. L. Rao, B. Karmakar and S. K. Biswas, *J. Alloys Compd.*, 2014, **583**, 498–509.
57 S. Karthik, S. G. Menon, D. N. Hebbar, K. S. Choudhari, C. Santhosh and S. D. Kulkarni, *Mater. Res. Bull.*, 2017, **94**, 513–519.
58 K.-C. Lee, S.-J. Lin, C.-H. Lin, C.-S. Tsai and Y.-J. Lu, *Surf. Coat. Technol.*, 2008, **202**, 5339–5342.
59 H. Baida, P. Billaud, S. Marhaba, D. Christofilos, E. Cottancin, A. Crut, J. Lermé, P. Maioli, M. Pellarin, M. Broyer, N. Del Fatti, F. Vallée, A. Sánchez-Iglesias, I. Pastoriza-Santos and L. M. Liz-Marzán, *Nano Lett.*, 2009, **9**, 3463–3469.
60 R. K. Chava, *Noble Metal-Metal Oxide Hybrid Nanoparticles*, Elsevier, 2019, pp. 499–516.
61 R. F. Aroca, *Phys. Chem. Chem. Phys.*, 2013, **15**, 5355.
62 M. J.-R. Previte, K. Aslan, Y. Zhang and C. D. Geddes, *Chem. Phys. Lett.*, 2006, **432**, 610–615.
63 J. F. Li, Y. F. Huang, Y. Ding, Z. L. Yang, S. B. Li, X. S. Zhou, F. R. Fan, W. Zhang, Z. Y. Zhou, D. Y. Wu, B. Ren, Z. L. Wang and Z. Q. Tian, *Nature*, 2010, **464**, 392–395.
64 O. Kulakovich, N. Strekal, A. Yaroshevich, S. Maskevich, S. Gaponenko, I. Nabiev, U. Woggon and M. Artemyev, *Nano Lett.*, 2002, **2**, 1449–1452.
65 V. Zucolotto, K. M. Gattás-Asfura, T. Tumolo, A. C. Perinotto, P. A. Antunes, C. J.-L. Constantino, M. S. Baptista, R. M. Leblanc and O. N. Oliveira, *Appl. Surf. Sci.*, 2005, **246**, 397–402.
66 K. Ray, R. Badugu and J. R. Lakowicz, *Chem. Mater.*, 2007, **19**, 5902–5909.
67 D. S. dos Santos, Jr. and R. F. Aroca, *Analyst*, 2007, **132**, 450.
68 R. F. Aroca, G. Y. Teo, H. Mohan, A. R. Guerrero, P. Albella and F. Moreno, *J. Phys. Chem. C*, 2011, **115**, 20419–20424.
69 A. R. Guerrero and R. F. Aroca, *Angew. Chem., Int. Ed.*, 2011, **50**, 665–668.
70 J. R. Lakowicz, G. Laczko, H. Cherek, E. Gratton and M. Limkeman, *Biophys. J.*, 1984, **46**, 463–477.
71 J. R. Lakowicz, Y. Shen, S. D'Auria, J. Malicka, J. Fang, Z. Gryczynski and I. Gryczynski, *Anal. Biochem.*, 2002, **301**, 261–277.
72 J. R. Lakowicz, *Principles of Fluorescence Spectroscopy*, Springer US, Boston, MA, 3rd edn, 2006.

73 V. Vargas, *J. Phys. Chem. A*, 2004, **108**, 281–288.
74 H. Aizawa, N. Ohishi, S. Ogawa, E. Watanabe, T. Katsumata, S. Komuro, T. Morikawa and E. Toba, *Rev. Sci. Instrum.*, 2002, **73**, 3089–3092.
75 P. Głuchowski, R. Pązik, D. Hreniak and W. Stręk, *Chem. Phys.*, 2009, **358**, 52–56.
76 D. Kleppner, *Phys. Rev. Lett.*, 1981, **47**, 233–236.
77 E. Yablonovitch, *Phys. Rev. Lett.*, 1987, **58**, 2059–2062.
78 S. Haroche and D. Kleppner, *Phys. Today*, 1989, **42**, 24–30.
79 C. Sönnichsen, T. Franzl, T. Wilk, G. von Plessen, J. Feldmann, O. Wilson and P. Mulvaney, *Phys. Rev. Lett.*, 2002, **88**, 774021.
80 A. Alabastri, S. Tuccio, A. Giugni, A. Toma, C. Liberale, G. Das, F. De Angelis, E. Di Fabrizio and R. P. Zaccaria, *Materials*, 2013, **6**, 4879–4910.
81 S. Link and M. A. El-Sayed, *Annu. Rev. Phys. Chem.*, 2003, **54**, 331–366.
82 C. Voisin, N. Del Fatti, D. Christofilos and F. Vallee, *J. Phys. Chem. B*, 2001, **105**, 2264–2280.
83 K. O. Aruda, M. Tagliazucchi, C. M. Sweeney, D. C. Hannah, G. C. Schatz and E. A. Weiss, *Proc. Natl. Acad. Sci. U. S. A.*, 2013, **110**, 4212–4217.
84 J. L. Montaño-Priede, O. Peña-Rodríguez and U. Pal, *J. Phys. Chem. C*, 2017, **121**, 23062–23071.
85 R. Gill and E. C. Le Ru, *Phys. Chem. Chem. Phys.*, 2011, **13**, 16366.